Helical quantum two-body problem and its wave packet dynamics

Peter Schmelcher*
Zentrum für Optische Quantentechnologien, Fachbereich Physik, Universität Hamburg, Luruper Chaussee 149, 22761 Hamburg, Germany

(Received 10 March 2026; accepted 18 May 2026; published 29 May 2026)

We explore the helical quantum two-body problem, i.e., two repulsively Coulomb interacting particles confined to move along a helix. The effective potential possesses a tunable number of potential wells superimposed on the repulsive Coulomb interaction that can be varied by changing the ratio of the pitch and radius of the helix. The anharmonicity of these wells depends crucially on this ratio and on the order of the well, which can also be seen by analyzing the individual wells' energy eigenvalue spacing. Our main focus is the investigation of the quantum dynamics of differently prepared wave packets that scatter from the multiwell potential landscape. We show that there exists a rich pattern-forming transient evolution that depends also on the number of bound states of the individual wells. We demonstrate how the multiple wells leave their fingerprints in the dynamics leading, among others, to oscillatory structures on different spatial scales, the formation of beats, and pulsed emission from single well localized wave packets due to their intrawell dynamics.

DOI: 10.1103/hh2r-zqdl

I. INTRODUCTION

Helical structures appear in a variety of different biological, chemical, and physical settings. One of the most prominent examples is certainly the double helix of the deoxyribonucleic acid due to the outstanding role this polymer plays for most organisms. Apart from DNA, important naturally occurring helical structures include α-helices in proteins, among many others. Here, helical structures are often related to certain functionalities arising from the specific geometry, such as biological information storage or cell proliferation [1]. A further example is the relationship between chirality of a molecule and its function [2]. Apart from naturally occurring helices, the controlled preparation and assembly of nanoscale helices is an intense field of research [3,4]. Possible fields of applications of nanohelices include, among others, optoelectronics [5], sensors [6], responsive materials [7], logic devices [8,9], single-molecule electronics [10], and nanoscale machines [11]. Specifically, helical carbon nanotubes for helix radii as small as $\approx$20 nm have been prepared in the laboratory [12]. Helical structures are also encountered in the realm of cold and ultracold trapped ions and neutral atoms. Harmonically confined ions can self-organize into intertwining helical arrays [13–19]. Ultracold neutral atoms can be trapped in the evanescent light fields emerging from a nanoscale optical fiber [20–22]. Here, the trapping light focuses winds in a helical manner around the fiber and can serve as a wave guide for either neutral atoms or dipolarly interacting atoms/molecules.

*Contact author: peter.schmelcher@uni-hamburg.de

Published by the American Physical Society under the terms of the Creative Commons Attribution 4.0 International license. Further distribution of this work must maintain attribution to the author(s) and the published article's title, journal citation, and DOI.

The above-described helical configurations have been one of the motivations for the development of a helical charged particle model. In this model, the charged particles are confined/constrained to move along a one-dimensional helix while interacting via the dynamically forbidden three-dimensional (3D) space. This model has been shown to exhibit several unusual and interesting properties in terms of both the resulting structures and dynamical behavior. First of all, the effective two-body interaction among the particles appears to be of oscillatory character and the purely repulsive character of the 3D Coulomb interaction can now develop local potential wells [23,24]. The number of those wells is finite and depends on the pitch and radius of the helical confinement. For two particles, the stable equilibria are formed by positioning the particles (approximately) at opposite sides of the winding of the helix; i.e., they form a displaced configuration. Increasing the number of equilibria and number of particles rapidly leads to a very complex many-body potential landscape that "lives" between regularity and randomness, thereby showing clustering behavior [25] evolving with increasing particle number.

Several investigations of the helical few- to many-body behavior have been performed in the past decade. In Ref. [26], the evolution of the classical band structure on a toroidal helix with varying helical radius has been explored, thereby unraveling a route to degeneracy and band inversion followed by a bifurcation from a single- to two-band structure [26]. The extension to the regime of nonlinear excitation dynamics [27] demonstrated a crossover from dispersion and revival dynamics in the lattice to "fragmentation" into breatherlike excitations. Adding external forcing and dissipation, the existence of a structural crossover and a pinned-to-sliding transition [28] has been found. The electrostatic bending response of a chain of particles on a finite helical filament shows a rich anomalous behavior depending on the geometry parameters, the filling, and the size [29]. In Ref. [30], the impact of an external electric field on the equilibria has been addressed and it was shown how the field can be used for state transfer. More recently, it has been demonstrated [31] that the electric field can also be employed to trigger a crossover from amorphous to crystalline order in the helical particle configurations. Driving the system with a time-dependent external field allows to split the chaotic phase space region, which has a strong impact on the direction of the resulting transport [32]. Augmenting this setup with a static field, one could show that the single-particle physics represents that of a generalization of the Kapitza pendulum [33].

While all of these investigations of helically confined Coulomb interacting particles are on their classical properties and dynamics, there is no *ab initio* investigation of the corresponding quantum properties and dynamics up to date. It is only for dipolarly anisotropically interacting particles that there exist a very few works on their bound states [34–36]. The present work aims at performing a first step in order to address this gap by exploring the helical quantum two-body problem. After establishing the quantum two-body Hamiltonian, we will analyze the properties of the underlying effective potential $\mathcal{V}$, thereby addressing the number and shape of individual potential wells occurring in $\mathcal{V}$. This includes a concise inspection of the spectrum of bound states for these (isolated) individual wells, which appear to be only metastable states with a finite lifetime as they occur in $\mathcal{V}$. The main results of this work concern the wave packet (WP) quantum dynamics of the two-body problem taking place in the highly oscillatory helical potential landscape. We explore the time evolution of the density of the wave packets (DWP) for different helical potentials with varying number of potential wells and demonstrate its dependence on the placement of the initial WP. Our focus is hereby on the intermediate time evolution and not on the asymptotic $t \to \infty$ behavior. The initial Gaussian undergoes a very rich pattern-forming interference dynamics, including, among others, pulses with multiple beats or a regular to irregular sequence of peaks. A rich intrawell versus interwell dynamics is unraveled leading to the interplay of fragmentation, above-barrier, and tunneling dynamics. The dynamics is also analyzed by exploring the time evolution of the occupation of the different individual wells as well as expectation values and mean-square displacements of the intrawell dynamics.

We proceed as follows. In Sec. II, we introduce our setup and Hamiltonian and discuss the properties of the oscillatory helical potential. In Sec. III, the shape of individual wells and their spectral properties are discussed. Section IV contains an analysis of the density evolution of WPs

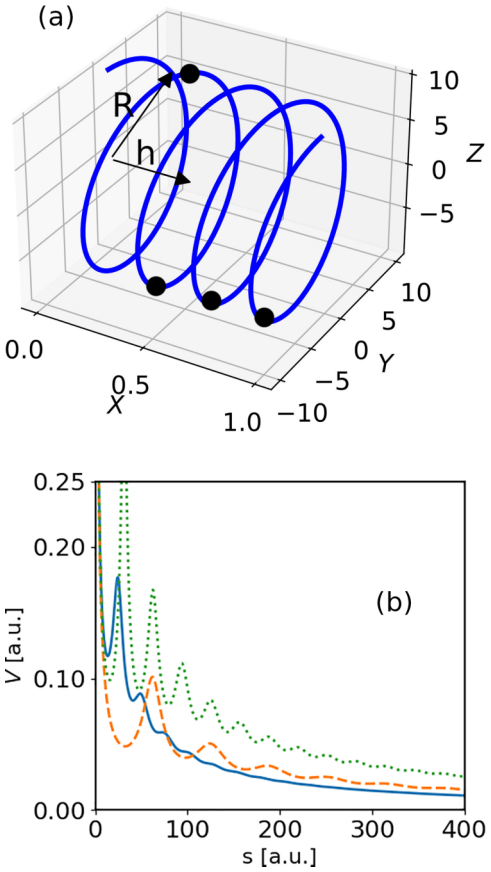


FIG. 1. (a) Sketch of a helix with the radius R and pitch h. The black spheres on the helix indicate equilibria of two particle positions: If one particle is on the top of the winding, the other is approximately at the bottom of the next or all following windings. Whether such a configuration represents a minimum and consequently forms a potential well depends on the detailed values of the radius and pitch (see text). (b) The helical potential V as a function of the path length s for three cases: $h = 5.8, R = 4$ (solid line, 3 potential wells), $h = 10, R = 10$ (dashed line, 6 potential wells), and $h = 3, R = 5$ (dotted line, 17 potential wells, not all shown).

with different initial conditions and for two different Hamiltonians. We also explore the time evolution of the resulting occupation probability of individual wells and the corresponding intrawell dynamics. Finally, in Sec. V we provide our conclusions and outlook.

II. SETUP AND HAMILTONIAN

We assume our charged particles to be confined to a strictly one-dimensional helix with constant pitch h and radius R [see the sketch of Fig. 1(a)]. The helix is given by the locus of all points $(x, y, z) = (R \times \cos(\frac{2\pi t}{h}), R \times \sin(\frac{2\pi t}{h}), t)$ where, e.g., $t \in [0, h]$ describes one winding. It possesses a constant curvature and torsion. We parametrize the helix by its path length $s = \sqrt{1 + (\frac{2\pi R}{h})^2}\, t$. The single-particle kinetic energy on the strictly one-dimensional helix can be obtained from that of an infinitely thin wave guide (see Refs. [37–39]) and appears to be in the canonical form $\frac{1}{2M} p_k^2$, with $p = \frac{1}{i} \frac{\partial}{\partial s_k}$, where k is the particle index. We assume $\hbar = e = 1$ in the following, where e is the elementary charge.

Placing two equally charged particles with the same mass $M_1 = M_2 = M$ on the helix leads to the two-body Hamiltonian

$$\mathcal{H} = \frac{1}{2M}p_1^2 + \frac{1}{2M}p_2^2 + \mathcal{V}(s_1, s_2). \tag{1}$$

We now exploit the fact that the helix is the only curved manifold that shows a separation of the center of mass and relative motion for an interacting particle system [40]. Transforming from the path length coordinates and momenta s_i, p_i, $i = 1, 2$ to the corresponding relative and center of mass (c.m.) coordinates $s = s_1 - s_2$, $S = \frac{s_1+s_2}{2}$ yields for the Hamiltonian

$$\mathcal{H} = \frac{1}{4M}p_S^2 + \frac{1}{M}p_s^2 + \mathcal{V}(s). \tag{2}$$

The c.m. separates and the corresponding kinetic energy can therefore be neglected from here on. For the relative motion, we therefore arrive at our working Hamiltonian

$$\mathcal{H}_s = \frac{1}{M}p_s^2 + \mathcal{V}(s), \tag{3}$$

with

$$\mathcal{V} = \left(2R^2\left(1 - \cos\left(\frac{s}{\beta}\right)\right) + \left(\frac{h}{2\pi\beta}\right)^2 \times s^2\right)^{-\frac{1}{2}}, \tag{4}$$

with $\beta = \sqrt{(\frac{h}{2\pi})^2 + R^2}$. The helical potential $\mathcal{V}$ possesses, besides the Coulombic term $\propto s^2$, an oscillatory contribution $\propto \cos(\frac{s}{\beta})$ with a spatial frequency $\frac{1}{\beta}$, which, for certain parameter domains, leads to the existence of a number of local potential wells [24] as we shall summarize in the following. As a consequence of the helical confinement, the purely repulsive 3D Coulomb interaction therefore turns into an oscillatory potential landscape. The physical picture behind this behavior is the fact that the two-particle interaction energy is sufficiently lowered while placing the charges on opposite sides of corresponding windings, whereas it is raised if they are on the same sides of the windings [see the sketch in Fig. 1(a)]. Figure 1(b) shows the helical potentials for the cases $(h = 5.8, R = 4)$, $(h = 10, R = 10)$, and $(h = 3, R = 5)$. These potentials possess 3, 6, and 17 potential wells, respectively. Their depths decrease with increasing order, i.e., increasing value of s for $s > 0$. Each minimum corresponds classically to a stable equilibrium configuration that is accompanied by a phase-space region of librational motion. Note that minima [see Fig. 1(a)] correspond to configurations where the two particles are on opposite sides of either the same or different windings, whereas maxima mean that they are on the same side of different windings. Let us derive the criterion for the existence of extrema. $\frac{d\mathcal{V}}{ds} = 0$ yields

$$\sin\left(\frac{s}{\beta}\right) = -\left(\frac{h^2}{4\pi^2R^2\beta}\right)s. \tag{5}$$

For given (h, R), this implicit equation provides with a set of extrema values for s by determining the intersection points of the straight line with the sine function. The point of the emergence of extrema occurs for the case of the same derivative of the sine and the linear function. This leads to the relationship

$$s = \beta\sqrt{\left(\frac{4\pi^2R^2}{h^2}\right)^2 - 1} \tag{6}$$

and resultingly an implicit equation for the helix parameter values at which extrema emerge:

$$\cos\left(\sqrt{\left(\frac{4\pi^2R^2}{h^2}\right)^2 - 1}\right) = -\frac{h^2}{4\pi^2R^2}. \tag{7}$$

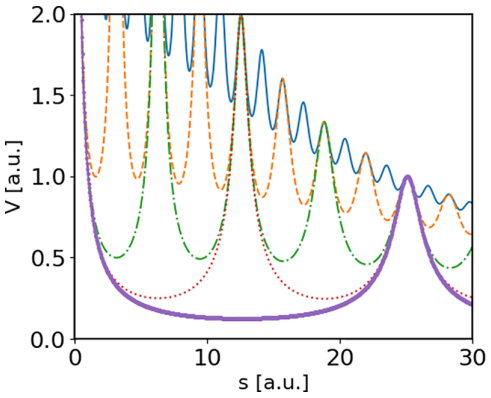


FIG. 2. A close-up into a specific window of the helical potential $\mathcal{V}$ as a function of the path length s for $h/R = 0.25$ for $R = 0.25, 0.5, 1.0, 2.0, 4.0$ corresponding to the solid, dashed, dot-dashed, dotted, and solid curves from top to bottom, in order to illustrate the appearance/shape of the individual potential wells.

Note that this relation depends only on the ratio $r = \frac{h}{R}$ and not on the values of the pitch and radius separately. The first few values of this ratio (bifurcation points) corresponding to the existence of one to five potential wells read $r \approx 2.929, 1.899, 1.513, 1.295, 1.151$. For $r \to 0$, we obtain approximately $\cos(\frac{4\pi^2}{r^2}) = 0$. This yields $r = \sqrt{\frac{8\pi}{2n+1}}$.

We note that performing a canonical scale transformation $s' = \frac{s}{\beta}$, $p'_s = \beta p_s$ yields the transformed Hamiltonian

$$H'_s \times M\beta^2 = p_s'^2 + \frac{2\pi M\beta^2}{h}\left(8\pi^2\frac{R^2}{h^2}(1-\cos(s')) + s'^2\right)^{-\frac{1}{2}}. \tag{8}$$

This shows that after performing the canonical scaling the potential term depends, apart from a prefactor $\frac{2\pi M\beta^2}{h}$, only on the ratio $\frac{h}{R}$ and not on h and R separately, with importance for the following discussion of individual well properties.

III. INDIVIDUAL WELL PROPERTIES AND SPECTRA

It is instructive to analyze the properties of individual wells of the potential $\mathcal{V}$. For that purpose, Fig. 2 shows a specific region of $\mathcal{V}(s)$ for $h/R = 0.25$ and different absolute values of (h, R). We observe that the extension of the potential wells changes from narrow to broad when increasing the values for both the pitch and the radius. Correspondingly, the positions of the minima increase with increasing helical parameter values. As analyzed above, decreasing $\frac{h}{R}$ means increasing the number of potential wells for a given interval of s. The individual wells are strongly anharmonic and it can be shown that this strong anharmonicity is maintained for changing (h, R) while keeping their ratio fixed (see Fig. 2) and, in particular, the scaling analysis of the previous section. Changing the ratio $\frac{h}{R}$ from values smaller than 1 to values larger than 1 decreases the degree of anharmonicity, as a corresponding quantitative analysis shows, and the harmonic approximation becomes increasingly valid. One should, however, keep in mind that individual wells are never parity symmetric around their minimum such that there is always a systematic deviation from a harmonic approximation. For given values of h and R, the anharmonicity increases with the order of the individual well; i.e., outer wells are systematically more anharmonic as compared to inner wells. At the same time, the depth of the wells decreases monotonically with their order: The deepest (shallowest) wells are the innermost (outermost) ones.

In the spirit of our analysis of individual wells, let us now inspect exemplarily the spectral properties of individual isolated wells. We therefore cut out individual wells from the helical potential $\mathcal{V}$ by setting the value of the potential $\mathcal{V}$ constant to the left and right of the position s where it reaches

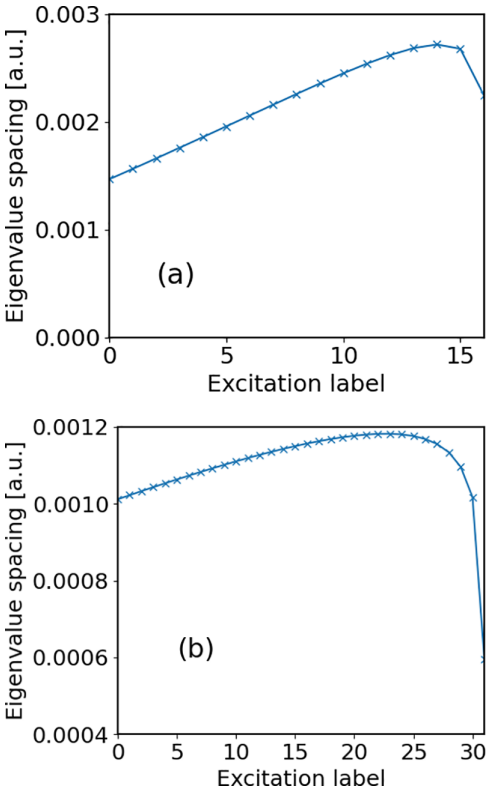


FIG. 3. (a) Energy eigenvalue spacing in the isolated innermost well of the helical potential $\mathcal{V}$ for $h = 20, R = 20, M = 1$. The eigenvalue spacing increases linearly for the 18 bound states except at the threshold to unboundedness. (b) The same but for the parameter values with $h = 12.2, R = 10, M = 100$, where 32 bound states exist. The linear slope is here much smaller, indicating the approximate equidistant spectrum.

the value of the energy maximum of the corresponding well. This way, the quasibound states of the wells of $\mathcal{V}$ become strictly bound states. We compute the spectra using a tenth-order finite difference discretization [41] and a corresponding diagonalization of the discretized Hamiltonian providing us with the eigenvalues and eigenvectors of the individual well problem.

Figure 3(a) shows the spacing of the discrete energy eigenvalues for the isolated innermost well of the helical potential $\mathcal{V}$ for $h = 20, R = 20$, and $M = 1$. The eigenvalue spacing increases approximately linearly with increasing degree of excitation for the first 13 spacings and consequently bends and starts to decrease for the very few states close to the potential threshold passing to the asymptotically constant behavior. We encounter approximately an increase of 100% of the spacing, which indicates that the spectrum belongs to a strongly anharmonic potential well. Figure 3(b) shows the eigenvalue spacing for the innermost well of the potential $\mathcal{V}$ for $h = 12.2, R = 10$, and $M = 100$, where 32 bound states exist. The linear slope is here much smaller, and the increase of the spacing is approximately 20%—This indicates that the anharmonicity of the underlying potential well is much weaker compared to the case of Fig. 3(a).

IV. QUANTUM DYNAMICS AND WAVE PACKET EVOLUTION

This section is dedicated to the analysis of the quantum dynamics in the helical potential by employing a Gaussian WP that is initially placed at different positions in the potential. Our goal is to demonstrate the variability in the dynamics due to interference, above-barrier, and tunneling effects

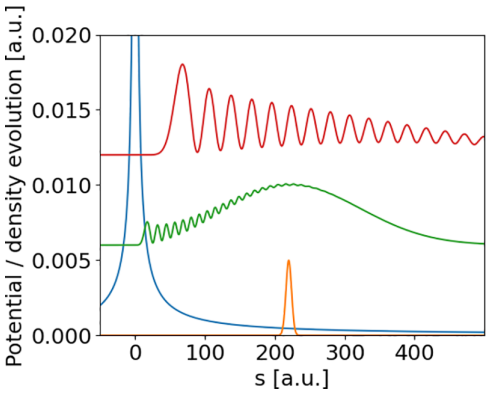


FIG. 4. The Coulomb potential and snapshots of the density time evolution for times $t = 0, 400, 1000$ (from bottom to top) for an initial Gaussian wave packet located at $s_0 = 220.0$ with zero momentum and width $\Delta s = 4.0$ for $M = 1$. The underlying sine-DVR grid has 2301 points in the interval $[-150, 1000]$. Note that both the potential and the densities are scaled (and shifted) to fit the same coordinate scale.

for different potentials and by using suitable analysis tools such as the individual well occupation (IWO) or intrawell expectation values. We emphasize that we do not address the asymptotic $t \to \infty$ scattering properties but are focusing on the intermediate time quantum dynamical behavior that illuminates the relevant processes taking place in the oscillatory potential surface.

A. Quantum dynamics in the helical landscape for $h = 5.8$, $R = 4$, $M = 1$

The helical potential for $h = 5.8, R = 4.0$ possesses three local potential wells with minima at positions $s \approx 13, 41, 69$. The (isolated) inner well is deep enough to accommodate for a single bound state, whereas the second and third wells possess no bound states, the latter being very shallow. We focus on the case $M = 1$ and cut off the helical potential sufficiently close to the singularity, such that the impact on all following results is marginal. Although originally designed for integrating the dynamics of many distinguishable (vibrational) modes, we use here the multiconfiguration time-dependent Hartree method (MCTDH), as well documented in Refs. [42–45], for integrating our underlying time-dependent Schrödinger equation. As a fundamental grid method, we use the sine discrete variable representation (DVR) with the typical number of grid points ranging between 2×10^3 and 4×10^3, thereby covering the coordinate s space such that the WP is well separated from the boundaries of the grid. As a result, we can work with open boundary conditions and no complex absorbing potentials are necessary.

Our initial ($t = 0$) WP reads

$$\Psi(s, t = 0) = \mathcal{N} \exp\left(-\frac{1}{4} \left(\frac{(s - s_0)}{\Delta s} \right)^2 \right) \exp(i p_0 (s - s_0)), \tag{9}$$

with the normalization $\mathcal{N} = (2\pi(\Delta s)^2)^{-\frac{1}{4}}$, the maximum position s_0, the width Δs, and the momentum p_0. To set the stage and for reasons of comparison, we remind the reader of what happens in the case of a pure Coulomb potential. Figure 4 shows three snapshots of the density of the wave packet for $t = 0, 400, 10^3$ from bottom to top for a WP with $s_0 = 220$, $\Delta s = 4.0$, $p_0 = 0$. At $t = 400$, due to reflection at the repulsive Coulomb potential, the onset of an oscillatory behavior on top of the left branch of the Gaussian envelope is observed. At $t = 10^3$, the DWP has largely reshaped into a backreflected oscillatory pulse with a monotonically decaying envelope structure. The approximately constant wavelength of the oscillations is determined by the magnitude of the momentum of the initial WP. With increasing time, this pulse roles down the Coulomb potential toward larger values of s while maintaining its shape during time evolution but increasing the wavelength and decreasing the amplitude of its spatial oscillations.

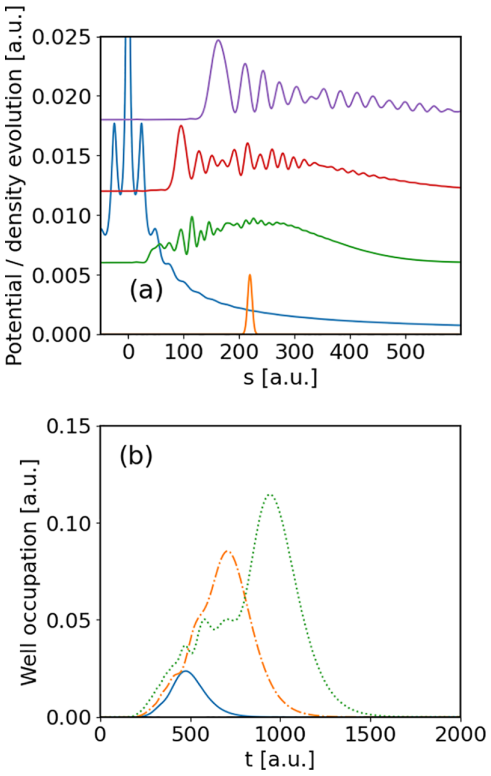


FIG. 5. (a) The helical potential ($h = 5.8, R = 4.0$) possessing three distinct minima and snapshots of the density time evolution for times $t = 0, 500, 700, 1000$ (from bottom to top) for an initial Gaussian wave packet located at $s_0 = 220.0$ with zero momentum and width $\Delta s = 4.0$ for $M = 1$. The underlying sine-DVR grid has 2301 points in the interval $[-150, 1000]$. Note that both the potential and the densities are scaled (and shifted) to fit the same coordinate scale. (b) The evolution of the density integrated over the first innermost (solid line), second (dash-dotted line), and third outermost (dotted line) wells of the potential.

We use again the above initial WP but now expose it to the helical potential for $h = 5.8, R = 4$. Our choice $s_0 = 220$ means that the initial WP is localized practically completely outside the regime of the potential wells. It should be noted that all below given density snapshots are, for each time evolution, scaled with different scaling factors in order to fit into a single figure. Our first focus is on zero-momentum initial WP to probe the helical potential landscape. Figure 5(a) shows the snapshots of the DWP for $t = 0, 500, 700, 10^3$. Upon the spreading of the left branch of the originally Gaussian WP toward the helical potential and its wells, we observe the formation of an oscillatory structure, like in the above pure Coulomb case, but now it exhibits a different substructure: We observe an envelope behavior with a nodal structure or, in other words, the emergence of a few beats in the developing density pulse. This pulse travels for longer times to larger distances while maintaining its overall structure but changing the corresponding amplitudes.

Figure 5(b) shows the corresponding time evolution of the populations or occupation, i.e., the integrated densities, between two maxima, i.e., each one covering an individual well (IWO) of the helical potential. As expected, the increase of the IWO with time happens first for the outermost followed by the inner wells. The innermost well possesses the smallest IWO, which decays at much earlier times compared to the two outer ones in the course of the dynamical WP reflection. The outermost well possesses the largest IWO for the longest time span. All IWOs exhibit a single dominant and broad peak, but the IWO of the outermost well presents an additional pronounced shoulder

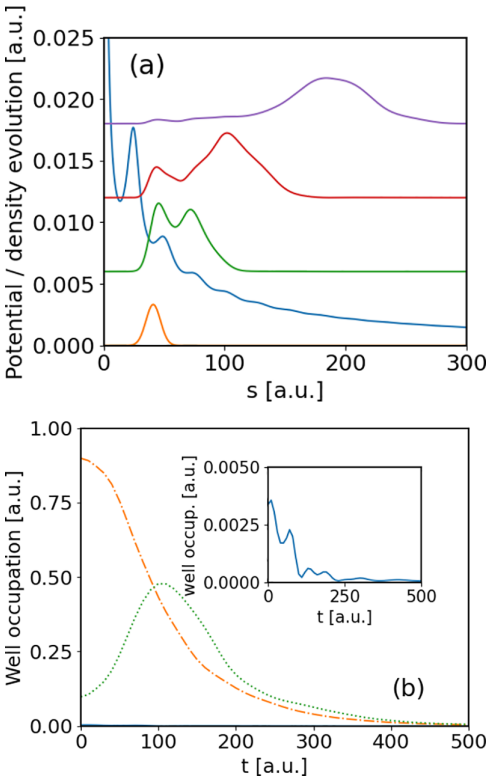


FIG. 6. (a) The helical potential ($h = 5.8$, $R = 4.0$) possessing three distinct minima and snapshots of the density time evolution for times $t = 0, 140, 230, 400$ (from bottom to top) for an initial Gaussian wave packet located at $s_0 = 40.99$ with zero momentum and width $\Delta s = 6.0$ and $M = 1$. The underlying sine-DVR grid has 2301 points in the interval $[-150, 1000]$. Note that both the potential and the densities are scaled (and shifted) to fit the same coordinate scale. (b) The evolution of the density integrated over the first innermost (solid line), second (dash-dotted line), and third outermost (dotted line) wells of the potential. The inset shows a close-up into the evolution of the integrated density for the first well.

for shorter times with small-amplitude oscillations on top. Comparing to the above-discussed Coulombic WP scattering, it is therefore evident already for this first study case that the presence of the wells in the helical potential leaves its fingerprints in the interference dynamics of the WP.

We now address the dynamical evolution of a WP that initially is centered at the minimum of the second to inner well, i.e., $s_0 = 40.99$, and possesses a width of $\Delta s = 6$. We remind the reader of the fact that this well possesses no (quasi)bound states.

Figure 6(a) shows the evolution of the DWP on the basis of snapshots for $t = 0, 140, 230, 400, 10^3$. At intermediate times, the originally single-humped DWP develops a broad double-peak structure where the first inner peak is roughly localized in the second inner well of the potential and the second peak is localized around the following third well; see the snapshot for $t = 140$. With increasing evolution time, the first peak decays and the second peak moves to larger distances; see the snapshot for $t = 230$. At $t = 400, 1000$, only an inner shallow tail of the density remains, while its single asymmetric broad peak moves outward to larger distances s. Figure 6(b) shows the corresponding IWO for the three wells. While the innermost well is only very weakly populated for short times (see inset), the second well possesses by preparation of the WP a dominant large IWO for $t = 0$, which decays monotonically with increasing time. The third outermost well has an approximately 10% IWO at $t = 0$ and increases thereafter.

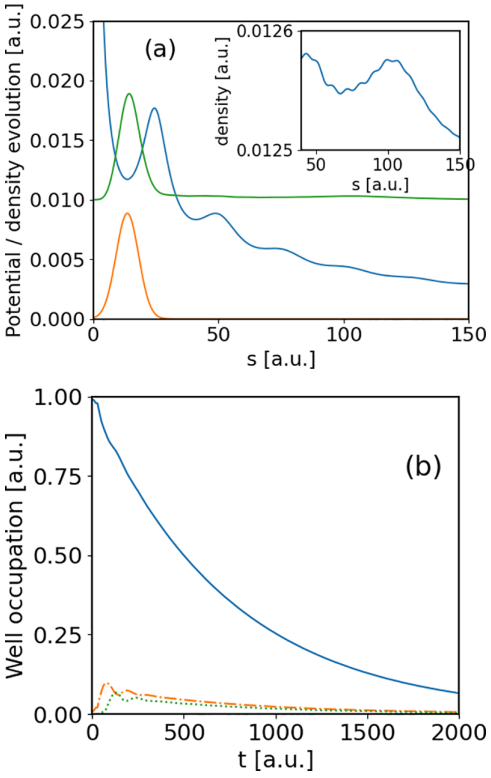


FIG. 7. (a) The helical potential ($h = 5.8, R = 4.0$) possessing three distinct minima and snapshots of the density time evolution for times $t = 0, 200$ (from bottom to top) for an initial Gaussian wave packet located at $s_0 = 13.63$ with zero momentum and width $\Delta s = 4.5$ for $M = 1$. The underlying sine-DVR grid has 3301 points in the interval $[-150, 1500]$. Note that both the potential and the densities are scaled (and shifted) to fit the same coordinate scale. The inset shows a close-up into the tail of the density distribution for $t = 200$. (b) The evolution of the density integrated over the first innermost (solid line), second (dash-dotted line), and third outermost (dotted line) wells of the potential.

At $t \approx 100$, the second and third wells possess the same IWO that represents (approximately) also the maximum probability in the time evolution of the third well. For large times $t > 300$, both IWOs became very small and are further decreasing according to a similar tail-like evolution. Obviously, this behavior is very distinct from the one shown above for the case $s_0 = 220$. As a natural next step, we explore the time evolution for an initial Gaussian WP centered at $s_0 = 13.63$, i.e., in the innermost well of the potential, for zero momentum, $M = 1$ and width $\Delta s = 4.5$. Figure 7(a) shows the corresponding snapshots for times $t = 0, 200$. The inset shows a close-up into the tail of the density distribution for $t = 200$. For such comparatively short times, there is a weak leaking of probability from the innermost well to large distances s. For longer times [see Fig. 7(b) up to $t = 2000$], there is a strong monotonous decrease of the inner well IWO such that for $t = 2000$ only 10% of the original probability is maintained. The small higher-order wells' IWO becomes largest for short times and decays thereafter very slowly on the mentioned large timescale.

Let us now consider the case of a finite (negative) momentum $p_0 = -0.154$ and relocating the initial WP back to $s_0 = 220$, i.e., far outside the region of the potential wells. Figure 8(a) shows the snapshots for the times $t = 550, 1000$. The scattering off the potential wells produces for intermediate times a DWP consisting of a main peak followed by two beats significantly different in amplitude; see snapshot for $t = 550$. For $t = 1000$, the beats are still present but the DWP has

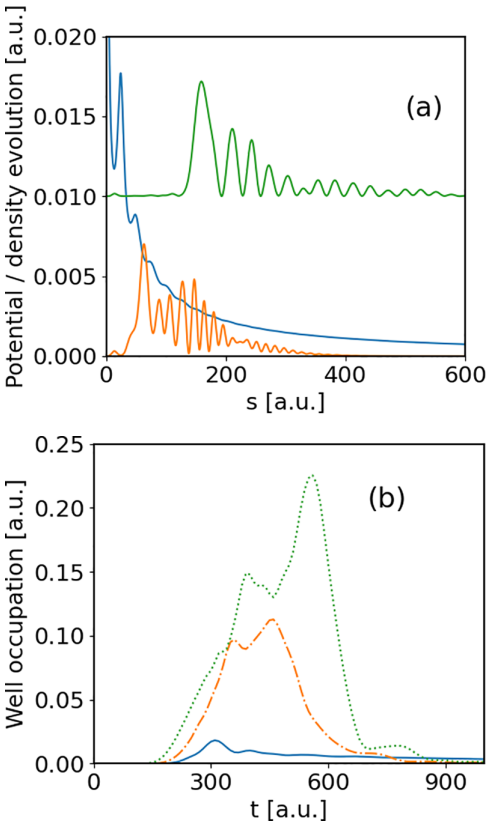


FIG. 8. (a) The helical potential ($h = 5.8, R = 4.0$) possessing three distinct minima and snapshots of the density time evolution for times $t = 550, 1000$ (from bottom to top) for an initial Gaussian wave packet located at $s_0 = 220.0$ with momentum $p_0 = -0.154$ ($M = 1$) and width $\Delta s = 4.5$. The underlying sine-DVR grid has 3301 points in the interval $[-150, 1500]$. Note that both the potential and the densities are scaled (and shifted) to fit the same coordinate scale. (b) The evolution of the density integrated over the first innermost (solid line), second (dash-dotted line), and third outermost (dotted line) wells of the potential.

overall moved to larger distances. The IWOs [see Fig. 8(b)] show therefore substantial nonzero values for all three wells only for $200 < t < 700$ with a similar structure to the one shown above.

Finally, for the same helical potential ($h = 5.8$, $R = 4.0$), we choose a much higher energy for the WP by imposing the parameter values $p_0 = -0.8, s_0 = 220.0, \Delta s = 4.5$. Figure 9 shows two snapshots at times $t = 180, 310$. The WP possesses now sufficient energy to surpass the (regularized) Coulomb singularity. The time instant $t = 180$ shows an intermediate stage of the transmission process where the single broad peak of the transmitted part of the DWP is emerging while the backreflected part shows (due to the high energy) many short-wavelength oscillations that accumulate for small values of s. At $t = 310$, the transmitted and reflected WPs are spatially well separated and each one shows a single broad peak structure.

B. Quantum dynamics in the helical landscape for $h = 10, R = 10, M = 1$

This subsection is dedicated to the helical landscape for pitch and radius being $h = 10, R = 10$. It possesses six potential wells with minima at positions $s \approx 32.5, 98, 163, 229, 295, 361$. The innermost (isolated) well is deep enough to accommodate for five bound states, the second well for three states, and the third as well as the fourth well for a single state. All further outer wells

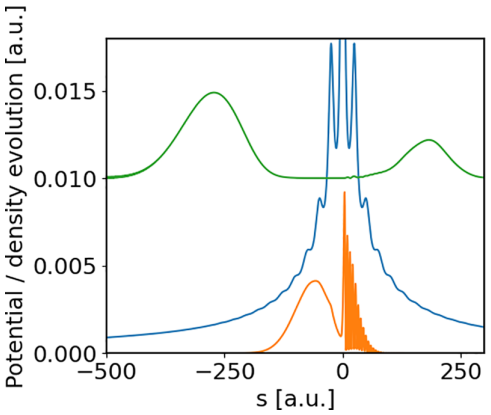


FIG. 9. The helical potential ($h = 5.8, R = 4.0$) possessing three distinct minima and snapshots of the density time evolution for times $t = 180, 310$ (from bottom to top) for an initial Gaussian wave packet located at $s_0 = 220.0$ with momentum $p_0 = -0.8$ and width $\Delta s = 4.5$ for $M = 1$. The underlying sine-DVR grid has 4001 points in the interval $[-500, 1500]$. Note that both the potential and the densities are scaled (and shifted) to fit the same coordinate scale.

have no bound states. Due to the existence of the larger number of wells as well as their few bound states, we expect a different phenomenology of the WP dynamics compared to the previous case $h = 5.8, R = 4.0$.

We start the study of the DWP evolution with an initial WP located at $s_0 = 350$, i.e., close to the minimum of the sixth well, for a width of $\Delta s = 4$ and zero momentum $p_0 = 0$. Figure 10(a) shows the snapshots of the evolution for the times $t = 600, 750, 1100, 1500$ and it becomes immediately evident that there is a more complex pattern formation in the DWP evolution. At $t = 600$, the density has still a main peak at $s_0 = 350$ but a very different shape for shorter as compared to large distances. For shorter distances, there are several oscillations equipped with smaller-amplitude higher-frequency suboscillations. For larger distances, the spreading of the DWP is smooth and monotonically decreasing: It does encounter neither the sequence of individual wells nor the (strongly) repulsive Coulomb branch. With further evolution time [see snapshots for $t = 750, 1100$ of Fig. 10(a)], the inner shorter-distance behavior of the DWP is restructured and passes through a period of reshaping the peaks, thereby encompassing a higher-frequency content. At $t = 1000$, three large main peaks are established followed, for larger distances, by a decaying tail with a regular oscillatory structure on top of it. For $t = 1500$, the DWP has developed into a pulse that shows, from short to large distances, a sequence of peaks with increasing height followed by a sequence of beats with decreasing amplitude. This structure travels with increasing time as a whole toward larger distances. Figure 10(b) shows the IWOs that, except for the innermost well IWO, all participate substantially in the scattering process. However, due to preparation, for short times the IWO of the sixth well is dominant but decreases rapidly with increasing time. For long times, the IWOs decrease step by step with their corresponding order.

Next our setup is the same initial WP like above, but we position it at $s_0 = 32.5$, which is the center of the first deep potential well. The DWP evolution is shown in Fig. 11(a) for $t = 0, 100, 200, 1000$. There is one main broad peak that persists for all time; i.e., the main part of the WP is trapped in the innermost well. However, it has a nontrivial dynamics and develops in a transient manner a double-peak structure. The corresponding IWO in Fig. 11(b) shows that the IWO for the innermost well decreases monotonically over the considered time interval from 1.0 to approximately 0.83.

Via the inset, it can be observed that this decay exhibits some substructure; i.e., it shows a sequence of mini plateaus that correspond to a "pulsed emission behavior" of the intrawell dynamics

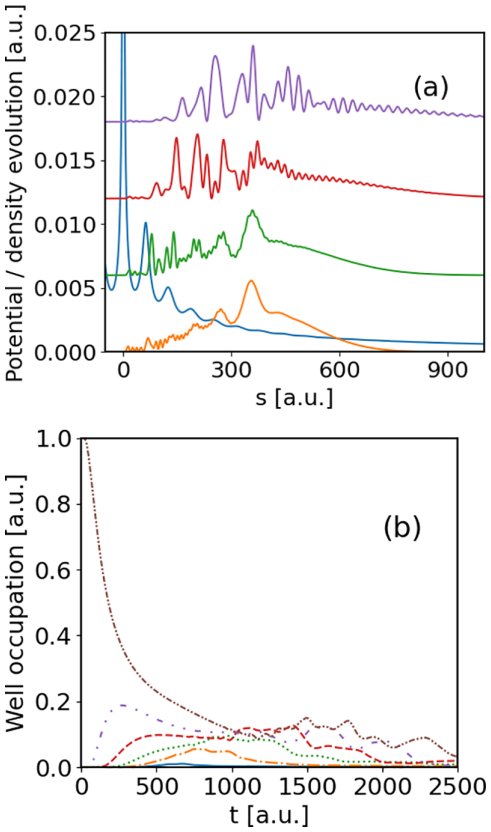


FIG. 10. (a) The helical potential ($h = 10, R = 10$) possessing six distinct minima and snapshots of the density time evolution for times $t = 600, 750, 1100, 1500$ (from bottom to top) for an initial Gaussian wave packet located at $s_0 = 350.0$ with zero momentum and width $\Delta s = 4$ for $M = 1$. The underlying sine-DVR grid has 4301 points in the interval $[-150, 2000]$. Note that both the potential and the densities are scaled (and shifted) to fit the same coordinate scale. (b) The evolution of the density integrated separately and individually over the first innermost to the sixth outermost well of the potential. The line styles for the first to the sixth integrated well probabilities are solid, dash dotted, dotted, dashed, dash dot dotted, and densely dash dot dotted.

of the first well. The second inset shows the behavior of the higher-order IWOs that show a steep short time raise in consecutive order followed by a tail. The latter reflects the mini plateau behavior upon closer inspection. Figures 11(c) and 11(d) address the intrawell dynamics by inspecting the (renormalized) expectation value $\langle s \rangle$, and the corresponding standard deviation $\sqrt{\langle s^2 \rangle - \langle s \rangle^2}$, respectively, as a function of time for all six wells. The evolution of the expectation values indicates that there is a center of mass motion taking place with varying amplitude from well to well. The innermost well center of mass dynamics possesses the smallest amplitude. The different oscillations are not synchronized and exhibit a slightly irregular character. For the standard deviation of the innermost well, we observe a very regular almost single-frequency oscillation around a mean value of eight indicating that a strong breathing dynamics takes place. For the second to the sixth well, the standard deviation dynamics shows an irregular short-time behavior followed an approximately single-frequency regular breathing dynamics around a mean value of 18 for longer times.

Figure 12(a) shows the DWP evolution for a case with nonzero negative initial momentum $p_0 = -0.3$ for the case $s_0 = 350.0$ at times $t = 940, 1500$. Again, we observe a rich transient structure formation in the pulse: At $t = 940$, we have for short distances a series of double peaks whose amplitudes increase with increasing distance s followed by several beats on top of a nonzero

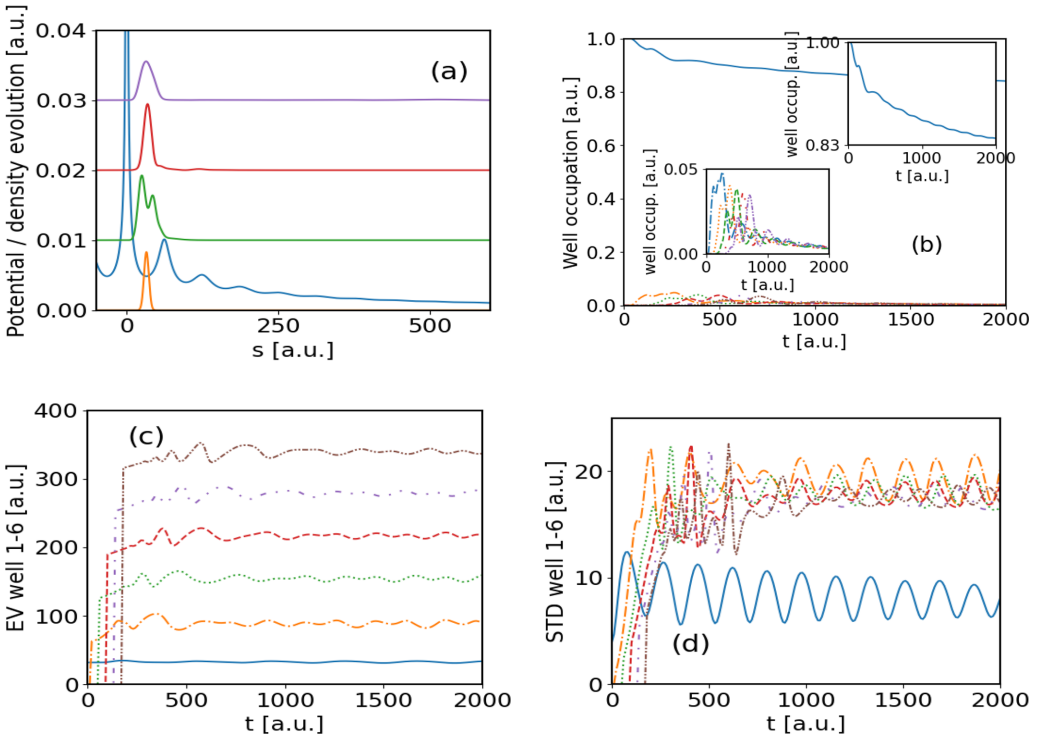


FIG. 11. (a) The helical potential ($h = 10, R = 10$) possessing six distinct minima and snapshots of the density time evolution for times $t = 0, 100, 200, 1000$ (from bottom to top) for an initial Gaussian wave packet located at $s_0 = 32.5$ with zero momentum and width $\Delta s = 4$ for $M = 1$. The underlying sine-DVR grid has 3301 points in the interval $[-150, 1500]$. Note that both the potential and the densities are scaled (and shifted) to fit the same coordinate scale. (b) The evolution of the density integrated separately and individually over the first innermost to the sixth outermost well of the potential. The line styles for the first to the sixth well probabilities are solid, dash dotted, dotted, dashed, dash dot dotted, and densely dash dot dotted. The insets enlarge into relevant regimes of evolution to identify the corresponding behavior. Panels (c) and (d) show observables of the intrawell dynamics: The expectation values of the coordinate s and its standard deviation, respectively, as a function of time for the six individual wells. Line style as in panel (b).

background. At later times $t = 1500$, this pulse has changed its appearance and shows now several stretched much broader humps with multiple sharp peaks on top followed by a background that exhibits small-amplitude undulations. The IWOs in Fig. 12(b) show now a much more complex oscillatory behavior reflecting the DWPs' structure formation: Upon a first rise in the course of the WP propagation, multiple suboscillations can be encountered changing the detailed profile of the decreasing envelope for all IWOs.

C. Quantum dynamics in the helical landscape for $h = 10, R = 10, M = 10$

So far we have been focusing on the case $M = 1$, but the mass is an important parameter for determining the number of bound states in the individual wells. To increase the latter, we consider now the situation $M = 10$ for the helix with $h = 10, R = 10$, i.e., for six wells. Then, the first to the sixth (isolated) well possess 14, 7, 2, 2, 2, and 0 bound states, respectively. We therefore expect a rich time evolution with a pattern-forming interference-based wave packet dynamics.

Figure 13(a) shows the DWP evolution for the times $t = 1800, 2500, 5000$ for an initial WP located at $s_0 = 350$ with zero momentum and width $\Delta s = 1.2$. At $t = 1800$, there is, analogously to the above case for $M = 1$ and the same helical landscape, a dominant central broad peak. Toward

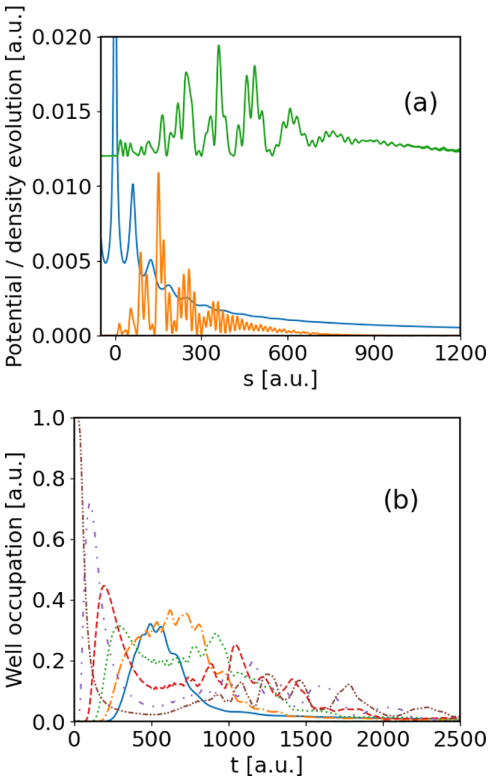


FIG. 12. (a) The helical potential ($h = 10, R = 10$) possessing six distinct minima and snapshots of the density time evolution for times $t = 940, 1500$ (from bottom to top) for an initial Gaussian wave packet located at $s_0 = 350.0$ with momentum $p_0 = -0.3$ and width $\Delta s = 4$ for $M = 1$. The underlying sine-DVR grid has 3301 points in the interval $[-150, 1500]$. Note that both the potential and the densities are scaled (and shifted) to fit the same coordinate scale. (b) The evolution of the density integrated separately and individually over the first innermost to the sixth outermost well of the potential. The line styles for the first to the sixth well probabilities are solid, dash dotted, dotted, dashed, dash dot dotted, and densely dash dot dotted.

larger distances, we have a smooth decay but for shorter distances the well structure of the potential leaves its fingerprints in the oscillations of the DWP.

Additionally, there is now a dense very high frequency modulation superimposed on the DWP with moderate amplitude. At later times ($t = 2500$), the innermost part of the DWP starts restructuring on top of an increased amplitude modulation. Step by step in the time evolution, this happens for all oscillatory structures to the left of the main peak until we finally observe a complete reshaping of the pulse. From shorter to larger distances, the pulse has now a sequence of low-frequency modulated broak peaks with increasing amplitude followed by a very broad main peak, all with high-frequency superimposed undulations and a sequence of beats of low amplitude forming the tail of the DWP. Again, this structure moves to larger distances as a whole while roughly maintaining its shape for some transient intermediate times (not shown here). Figure 13(b) shows the evolution of the corresponding IWO being in all major aspects similar to the above-observed one for $M = 1$ with individual time evolutions, of course, differing.

It is now, for $M = 10$, instructive to explore the case for which the initial WP is centered in a potential well of the helical landscape, specifically the second well. To be concise, Fig. 14(a) shows a single snapshot at $t = 3000$ for the parameter values $s_0 = 98.0$ and $\Delta s = 1.2$. What we can observe in this DWP snapshot is a broad peak with a thin shoulder toward larger distances, which

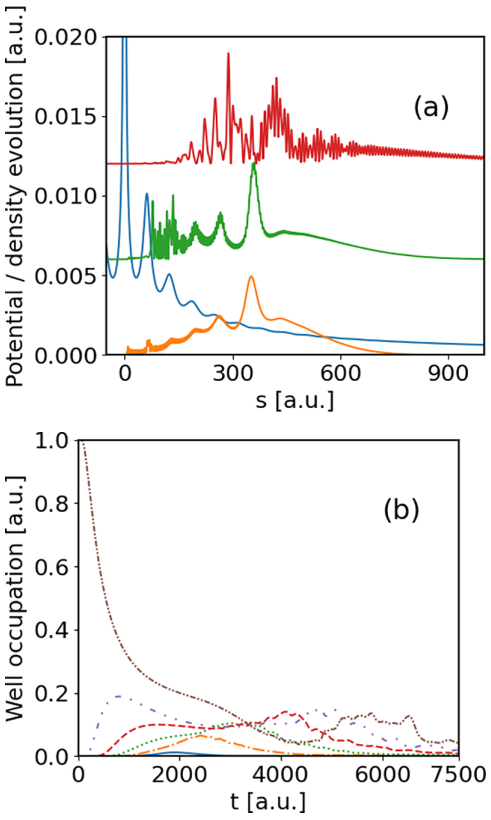


FIG. 13. (a) The helical potential ($h = 10, R = 10$) possessing six distinct minima and snapshots of the density time evolution for times $t = 1800, 2500, 5000$ (from bottom to top) for an initial Gaussian wave packet located at $s_0 = 350.0$ with zero momentum and width $\Delta s = 1.2$ for $M = 10$. The underlying sine-DVR grid has 3301 points in the interval $[-150, 1500]$. Note that both the potential and the densities are scaled (and shifted) to fit the same coordinate scale. (b) The evolution of the density integrated separately and individually over the first innermost to the sixth outermost well of the potential. The line styles for the first to the sixth well probabilities are solid, dash dotted, dotted, dashed, dash dot dotted, and densely dash dot dotted.

indicates the dynamics taking place in this second well of the major fraction of the WP remaining there within the finite time evolution considered here. Also clearly visible is the prominent pulse that has been emitted from the initial WP up to this time $t = 3000$ and is mainly localized in the domain $200 < s < 700$. It shows three central main peaks and, both left and right to them, a decaying profile with small-amplitude oscillations on top.

Since this is only a snapshot, further intriguing dynamics happens in the course of the time evolution, as can be seen from the IWO dynamics in Fig. 14(b). First of all, the IWO for the first innermost well is overall small and only essentially nonzero for short times, which is a consequence of the still well-separated character of the innermost well from the outer ones for the given WP energy.

The dominant IWO for the second well rapidly decays from the initial value very close to one, and this decay slows temporarily down around $t \approx 800$ before it accelerates again and reaches out to an asymptote for $t > 2000$. But even during this long-time behavior [see inset in Fig. 14(b)], the second IWO shows a sequence of plateaus in its decay that stem from the pulsed emission of probability from the second well due to its internal dynamics (see below). The IWOs for the third and further outer wells up to the sixth well show a strong participation in the dynamics for the time interval $0 < t < 4000$. However, even beyond this time interval the corresponding inset in

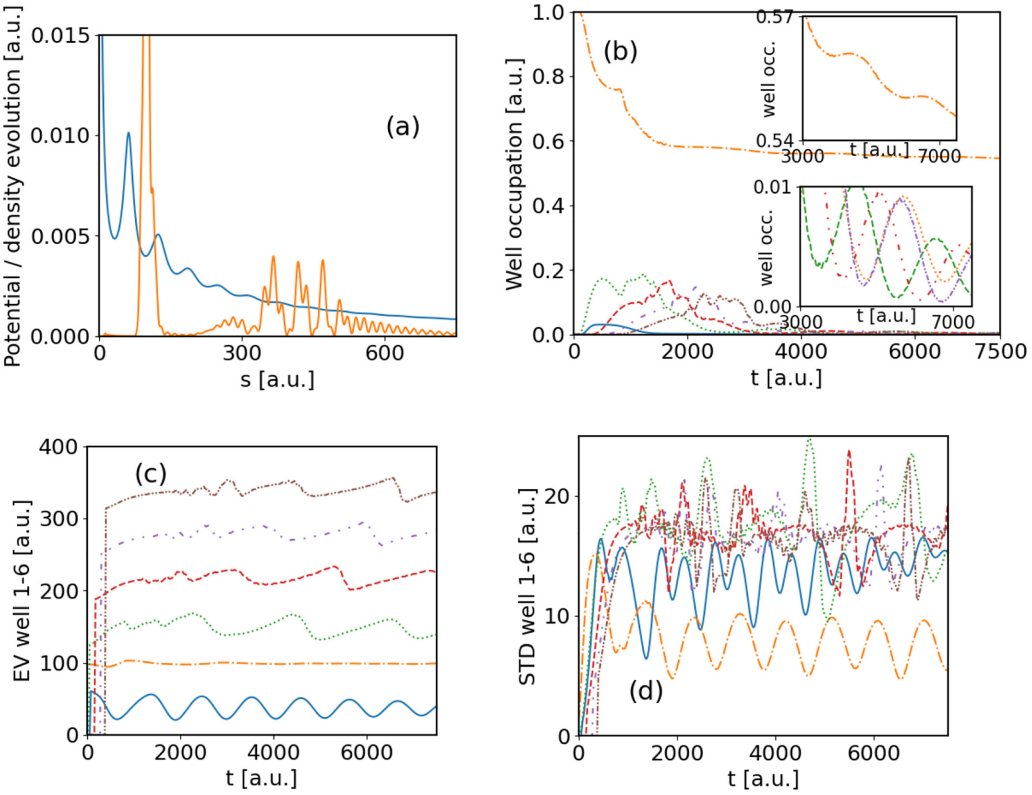


FIG. 14. (a) The helical potential ($h = 10, R = 10$) possessing six distinct minima and a snapshot of the density time evolution for time $t = 3000$ for an initial Gaussian wave packet located at $s_0 = 98.0$ with zero momentum and width $\Delta s = 1.2$ for $M = 10$. The underlying sine-DVR grid has 3301 points in the interval $[-150, 1500]$. Note that both the potential and the densities are scaled (and shifted) to fit the same coordinate scale. (b) The evolution of the density integrated separately and individually over the first innermost to the sixth outermost well of the potential. The line styles for the first to the sixth well probabilities are solid, dash dotted, dotted, dashed, dash dot dotted, and densely dash dot dotted. The two insets show close-ups into corresponding regions to identify the behavior. Panels (c) and (d) show observables of the intrawell dynamics: The expectation values of the coordinate s and its standard deviation, respectively, as a function of time for the six individual wells. Line style as in panel (b).

Fig. 14(b) demonstrates its interesting behavior: It exhibits oscillations with a certain phase relation related to their spatial separation. These oscillations are, of course, directly related to the previously mentioned pulsed emission from the IWO dynamics of the second well.

Figures 14(c) and 14(d) address the intrawell dynamics, i.e., the expectation values of the coordinate s and its standard deviation, respectively, as a function of time for the six individual wells. The expectation value of the innermost well shows a single-frequency harmonic oscillation, the second well shows almost no dynamics at all at least for not too short times, and the higher-order wells show similar very anharmonic oscillations with a strong asymmetry with respect to their forward (increasing $\langle s \rangle$) and backward (decreasing $\langle s \rangle$) motion. The standard deviation shows a few-mode dynamics for the first and second wells and a much more irregular multimode dynamics for the higher wells. On top of small-amplitude oscillations, there occur narrow peaks of intermittent dynamical character.

Finally, let us inspect the DWP evolution for a WP initially centered in the first innermost well with $s_0 = 32.5$ and $\Delta s = 1.2$. A snapshot for $t = 4100$ is shown in Fig. 15(a). The density

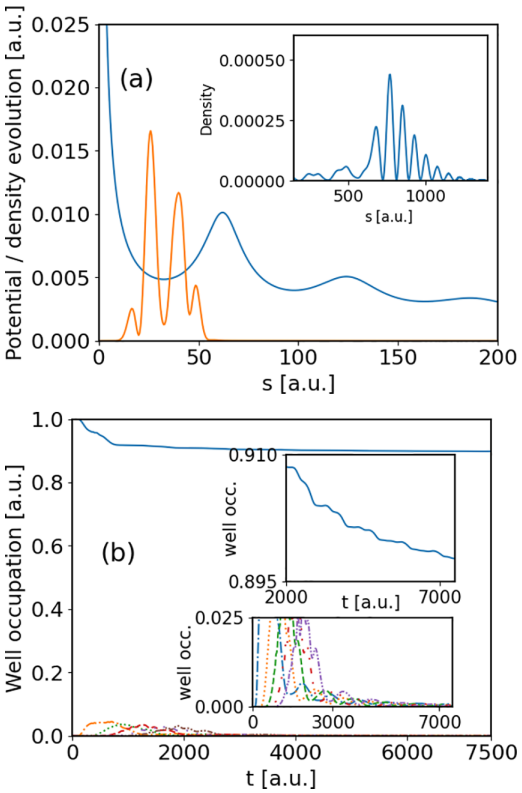


FIG. 15. (a) The helical potential ($h = 10, R = 10$) possessing six distinct minima and a snapshot of the density time evolution for time $t = 4100$ for an initial Gaussian wave packet located at $s_0 = 32.5$ with zero momentum and width $\Delta s = 1.2$ for $M = 10$. The underlying sine-DVR grid has 4001 points in the interval $[-500, 1500]$. Note that both the potential and the densities are scaled (and shifted) to fit the same coordinate scale. The inset shows a close-up into the tail of the wave packet to resolve its structure. (b) The evolution of the density integrated separately and individually over the first innermost to the sixth outermost well of the potential. The line styles for the first to the sixth well probabilities are solid, dash dotted, dotted, dashed, dash dot dotted, and densely dash dot dotted. The insets enlarge into relevant regimes to identify the underlying behavior.

profile in this first well now shows at this time multiple large-amplitude oscillations on top of a broad distribution. This, of course, heavily varies with changing time due to the strong internal well dynamics (see below). Again, the inset shows a pulse that has been emitted previously with low amplitude overall and characteristic shape, which is traveling with increasing time to larger distances. Other pulses do follow regularly, as can be seen from the corresponding IWOs in Fig. 15(b); see, in particular, the inset for the IWO evolution of the first well showing a characteristic plateau structure. The IWOs of the second to higher wells are, compared to the case of Fig. 14, somewhat suppressed but they exhibit a similar characteristic behavior, as seen in the corresponding inset of Fig. 15(b).

V. CONCLUSIONS AND OUTLOOK

The idea of exploring long-range interacting particle systems on curved manifolds for which the particles are dynamically constrained to move on a lower-dimensional surface but interact via the entire three-dimensional space has by now proven to lead to a variety of interesting structures

and phenomena, as well as an intriguing dynamics [24–37,40]. However, the absolute majority of these works are for classical particle systems and we present here the first exploration of the quantum two-body problem for two charged particles on a helix. The helix is of particular interest for several reasons: Due to the constant curvature and torsion, (1) it allows for a simple quantum Hamiltonian structure, (2) it leads to a separation of the center of mass and internal motion, and (3) the tunable number of (classically stable) equilibria and wells leads to rich structural, and consequently dynamical, characteristics between symmetry-dominated order and complete disorder. For the repulsive two-body problem, this implies that the equilibria of the two particles are (approximately) on opposite sides of the same or different windings. For more particles, this picture is systematically modified and enhanced and leads to an intriguing cluster formation [25].

Here, we perform the first steps toward an understanding of the quantum properties of repulsively interacting helical particle systems at hand of the two-body case that reduces, after separation of the center of mass, to a pure relative motion problem. It turns out that, additionally to the well-known fact that the number of potential wells can be changed by tuning the pitch h and radius R, the anharmonicity of the individual wells varies strongly. The relevant parameter to change the degree of anharmonicity is $\frac{h}{R}$ and, besides this, the order of the well in a given helical potential. Correspondingly, we inspected the individual (isolated) wells' spectra and found that the energy eigenvalue spacing can be approximately constant, i.e., harmonic oscillatorlike, over a broad range of excitations to strongly increasing due to a strong anharmonicity.

The main theme of this work is the study of the quantum dynamics, i.e., time evolution of wave packets with varying location in the multiwell potential landscape, varying width and momentum. We have hereby been focusing on two setups with three versus six potential wells. We also considered both cases $M = 1$ and $M = 10$. For $M = 1$, the setup with $h = 5.8$, $R = 4.0$ (three wells) possesses a single bound state for the isolated inner well and none for the outer ones. This case was, in a nutshell, the one with the, compared to the other cases, least complex quantum dynamics. Nevertheless, we observed a restructuring of the wave packet and the formation of beats or simply a fragmentation of the wave packet upon initially localizing it between two wells. The tunneling out of a well appeared to be rather structureless, which is not unexpected due to the fact that the well had one or no bound states.

For the helical potential $h = 10$, $R = 10$, and $M = 1$ with six wells with a series of bound states and many for $M = 10$, the interference dynamics becomes significantly richer in pattern-forming pulses. For an initial WP located at large distances the latter are imprinted on the WP while spreading toward the repulsive Coulomb branch and exhibit additional short-wavelength smaller-amplitude oscillations. A major restructuring of this pulse occurs while completing the reflection dynamics into a sequence of broader peaks followed by a sequence of beats with decreasing amplitude, which then, transiently, travels as a complete pulse to larger distances. Locating the initial WP at an inner well leads to rich above-barrier and tunneling dynamics due to the intrawell dynamics: Pulse shaping is combined with an overall oscillating emission of them. We have analyzed these features, among others, by inspecting the individual well occupation and the intrawell dynamics.

Possible experimental preparations of helices are state-of-the-art nanostructure fabrication techniques based on self-organization or lithography. In this case, the electron or hole dynamics would be on the scale of tens/hundreds of nanometers. Ultracold trapped ions are a second promising candidate. Here, it would need a design of helical field configurations on the micrometer scale to trap the previously laser cooled atomic ions, thereby reaching sufficiently low temperatures to enter the quantum regime.

While the present work shows the variety of possibilities for the pattern- and pulse-shape-forming reflection dynamics in the collision of the two charged particles while propagating across the windings, it is only the beginning of the exploration of the helical quantum problem. An immediate next step would be the investigation of the more particle dynamics, which carries the promise of showing a variety of transient binding schemes and would involve many different pattern formation timescales. Alternatively and complementary to the present quantum dynamical approach, and in

order to compute the underlying resonances, i.e., their energetical positions and widths, a complex scaling approach might be developed and applied.

ACKNOWLEDGMENTS

The author acknowledges many helpful discussions with H. D. Meyer and A. Becker concerning the usage of the Heidelberg MCTDH software package. This work has been in part conducted during a visit to the Center for Theoretical Physics at Hainan University whose hospitality is greatly appreciated.

DATA AVAILABILITY

The data that support the findings of this article are not publicly available upon publication because it is not technically feasible and/or the cost of preparing, depositing, and hosting the data would be prohibitive within the terms of this research project. The data are available from the authors upon reasonable request.

[1] M. Ilamaran *et al.*, A self-assembly and higher order structure forming triple helical protein as a novel biomaterial for cell proliferation, Biomater. Sci. **7**, 2191 (2019).

[2] U. Meierhenrich, *Amino Acids and the Asymmetry of Life, Advances in Astrobiology and Biogeophysics* (Springer, Berlin, 2008).

[3] Z. Ren and P. X. Gao, A review of helical nanostructures: Growth theories, synthesis strategies and properties, Nanoscale **6**, 9366 (2014).

[4] A. Shaikjee and N. J. Coville, The synthesis, properties and uses of carbon materials with helical morphology, J. Adv. Res. **3**, 195 (2012).

[5] V. Percec *et al.*, Self-organization of supramolecular helical dendrimers into complex electronic materials, Nature (London) **419**, 384 (2002).

[6] E. Yashima *et al.*, Helical polymers: Synthesis, structures, and functions, Chem. Rev. **109**, 6102 (2009).

[7] D. Pijper and B. L. Feringa, Control of dynamic helicity at the macro- and supramolecular level, Soft Matter **4**, 1349 (2008).

[8] R. C. Merkle and K. E. Drexler, Helical logic, Nanotechnology **7**, 325 (1996).

[9] D. Das Gupta and S. K. Maiti, Implementation of logical operations using antiferromagnetic helical molecule, J. Phys. D: Appl. Phys. **56**, 465304 (2023).

[10] A. V. Malyshev, DNA double helices for single molecule electronics, Phys. Rev. Lett. **98**, 096801 (2007).

[11] J. Li *et al.*, Template electrosynthesis of tailored-made helical nanoswimmers, Nanoscale **6**, 9415 (2014).

[12] V. Ivanov *et al.*, The study of carbon nanotubules produced by catalytic method, Chem. Phys. Lett. **223**, 329 (1994).

[13] T. W. Hyde, K. Jong, and L. S. Matthews, Helical structures in vertically aligned dust particle chains in a complex plasma, Phys. Rev. E **87**, 053106 (2013).

[14] H. Landa *et al.*, Structure, dynamics and bifurcations of discrete solitons in trapped ion crystals, New J. Phys. **15**, 093003 (2013).

[15] N. G. Gusein-Zade, Helical structures in complex plasma I: Noncollective interaction, Plasma Phys. Rep. **31**, 392 (2005).

[16] V. N. Tsytovich, Helical structures in complex plasma II: Collective interaction, Plasma Phys. Rep. **31**, 824 (2005).

[17] G. Birkl, S. Kassner, and H. Walther, Multiple-shell structures of laser-cooled $^{24}Mg^{+}$ ions in a quadrupole storage ring, Nature (London) **357**, 310 (1992).

[18] J. J. Bollinger, D. J. Wineland, and D. H. E. Dubin, Non-neutral ion plasmas and crystals, laser cooling, and atomic clocks, Phys. Plasmas **1**, 1403 (1994).

[19] R. Hasse and J. Schiffer, The structure of the cylindrically confined Coulomb lattice, Ann. Phys. **203**, 419 (1990).

[20] D. Reitz and A. Rauschenbeutel, Nanofiber-based double-helix dipole trap for cold neutral atoms, Opt. Commun. **285**, 4705 (2012).
[21] E. Vetsch *et al.*, Optical interface created by laser-cooled atoms trapped in the evanescent field surrounding an optical nanofiber, Phys. Rev. Lett. **104**, 203603 (2010).
[22] E. Vetsch *et al.*, Nanofiber-based optical trapping of cold neutral atoms, IEEE **18**, 1763 (2012).
[23] O. Kibis, Electron-electron interaction in a spiral quantum wire, Phys. Lett. A **166**, 393 (1992).
[24] P. Schmelcher, Effective long-range interactions in confined curved dimensions, Europhys. Lett. **95**, 50005 (2011).
[25] J. M. Dörre, F. K. Diakonos, and P. Schmelcher, Long-range interacting particles on a helix: A statistical and correlation analysis of equilibrium configurations, Phys. Rev. E **112**, 054116 (2025).
[26] A. V. Zampetaki, J. Stockhofe, and P. Schmelcher, Degeneracy and inversion of band structure for Wigner crystals on a closed helix, Phys. Rev. A **91**, 023409 (2015).
[27] A. V. Zampetaki, J. Stockhofe, and P. Schmelcher, Dynamics of nonlinear excitations of helically confined charges, Phys. Rev. E **92**, 042905 (2015).
[28] A. V. Zampetaki, J. Stockhofe, and P. Schmelcher, Pinned-to-sliding transition and structural crossovers for helically confined charges, Phys. Rev. E **95**, 022205 (2017).
[29] A. V. Zampetaki, J. Stockhofe, and P. Schmelcher, Electrostatic bending response of a charged helix, Phys. Rev. E **97**, 042503 (2018).
[30] J. Plettenberg *et al.*, Local equilibria and state transfer of charged classical particles on a helix in an electric field, Phys. Rev. E **95**, 012213 (2017).
[31] A. Siemens and P. Schmelcher, Tunable order of helically confined charges, Phys. Rev. E **102**, 012147 (2020).
[32] A. Siemens and P. Schmelcher, External-field-induced dynamics of a charged particle on a closed helix, Phys. Rev. E **103**, 052217 (2021).
[33] J. F. Gloy, A. Siemens, and P. Schmelcher, Driven toroidal helix as a generalization of the Kapitza pendulum, Phys. Rev. E **105**, 054204 (2022).
[34] J. K. Pedersen *et al.*, Formation of classical crystals of dipolar particles in a helical geometry, J. Phys. B **47**, 165103 (2014).
[35] J. K. Pedersen *et al.*, Quantum few-body bound states of dipolar particles in a helical geometry, J. Phys. B **49**, 024002 (2016).
[36] J. K. Pedersen *et al.*, Quantum single-particle properties in a one-dimensional curved space, J. Mod. Opt. **63**, 1814 (2016).
[37] J. Stockhofe and P. Schmelcher, Nonadiabatic couplings and gauge-theoretical structure of curved quantum waveguides, Phys. Rev. A **89**, 033630 (2014).
[38] R. C. T. da Costa, Quantum mechanics of a constrained particle, Phys. Rev. A **23**, 1982 (1981).
[39] A. T. P. de Araujo and E. O. Silva, Quantum scattering in helically twisted geometries: Coulomb-like interaction and Aharonov-Bohm effect, arXiv:2602.05229.
[40] A. V. Zampetaki *et al.*, Classical scattering of charged particles confined on an inhomogeneous helix, Phys. Rev. E **88**, 043202 (2013).
[41] G. C. Groenenboom and H. M. Buck, Solving the discretized time-independent Schrödinger equation with the Lanczos procedure, J. Chem. Phys. **92**, 4374 (1990).
[42] H. D. Meyer, U. Manthe, and L. S. Cederbaum, The multi-configurational time-dependent Hartree approach, Chem. Phys. Lett. **165**, 73 (1990).
[43] U. Manthe, H. D. Meyer, and L. S. Cederbaum, Wave-packet dynamics within the multiconfiguration Hartree framework: General aspects and application to NOCl, J. Chem. Phys. **97**, 3199 (1992).
[44] M. H. Beck *et al.*, The multiconfiguration time-dependent Hartree (MCTDH) method: A highly efficient algorithm for propagating wavepackets, Phys. Rep. **324**, 1 (2000).
[45] *Multi-dimensional Quantum Dynamics: MCTDH Theory and Applications*, edited by H. D. Meyer, F. Gatti, and G. A. Worth (Wiley-VCH, Weinheim, 2009).